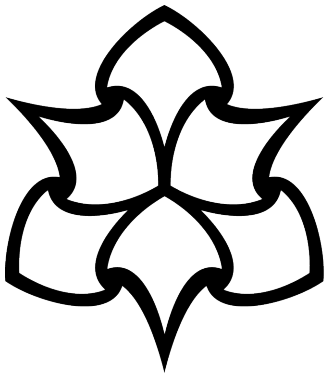

CRYSTAL GROWTH & DESIGN

Article

pubs.acs.org/crystal

Investigation of the Effect of Ultrasound Parameters on Continuous Sonocrystallization in a Millifluidic Device

Rashid Jamshidi,[†] Damiano Rossi,[†] Nader Saffari,[‡] Asterios Gavriilidis,[†] and Luca Mazzei*[,†]

[†]Department of Chemical Engineering and [‡]Department of Mechanical Engineering, University College London, Torrington Place, London WC1E 7JE, U.K.

ABSTRACT: Continuous-flow crystallization of adipic acid in a millichannel chip equipped with a piezoelectric element is presented and investigated experimentally and numerically. A single, straight channel chip (cross section: 2 mm × 5 mm, length: 76 mm) made of glass, which is ultrasonically transparent, was designed and fabricated. The piezoelectric element allows studying the effect of different ultrasound frequencies in the kHz to MHz range. Ultrasound was applied in burst mode to reduce heating; this allowed operating at higher levels of input power. To accurately control the temperature of the fluid, Peltier elements were used to cool the bottom and top surfaces of the chip. Crystallization was performed in isothermal conditions, ensuring that the temperature and in turn the supersaturation were kept uniform along the channel. The effect of ultrasound frequency and sonication time was studied. Crystal size distributions at different operating conditions were obtained by laser diffraction. The distributions were narrow, with coefficients of variation ∼0.5, while the mean sizes were small (∼30 μm) and decreased when the sonication time increased. The crystal production rate increased by increasing the sonication time; this suggests that ultrasound enhances nucleation. On the other hand, in crystal breakage experiments, no difference in the size distribution of the seed crystals entering and leaving the device was observed, and hence, in this setup, ultrasound does not cause breakage. Numerical simulations of wave propagation in aqueous solution were utilized to predict the probability of cavitation, adopting a suitable cavitation threshold. The simulations showed that high pressure amplitudes are achievable inside the channel at low frequencies. The size range of bubbles which undergo violent collapse at different pressure amplitudes and frequencies was quantified. By increasing the frequency in the simulations, it was observed that the probability of transient cavitation decreases. The theoretical prediction of negligible transient cavitation at higher frequencies, in conjunction with the absence of crystals at such frequencies, indicates a strong link between transient cavitation and sonocrystallization.

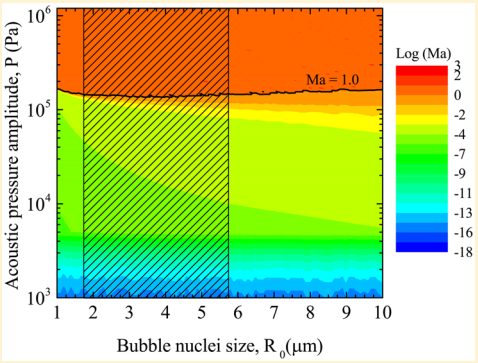

INTRODUCTION

Crystallization is a complex process involving multiphase equilibrium, polymorphic transformations, and nucleation and growth kinetics. This makes the prediction, design, and control of crystallization processes challenging. To improve crystallization product quality, in recent years there has been an increased interest in continuous-flow crystallizers. Despite the industrial benefits of batch crystallizers, continuous-flow ones offer a technology with the potential to form particles with excellent homogeneity and control the critical process parameters in a way that is difficult to achieve in batch crystallizers. Owing to the continuous nature of the process and more controllable fluid dynamic conditions, these systems require smaller volumes and lower operating and labor costs, offering improved controllability and reproducibility and therefore better control over particle size, shape, and crystallinity.[1]

Sonication, the application of power ultrasound to process fluids, is an intensification technology that, when applied to crystallization, permits tailoring and improving significantly both process and product quality.[2,3] The additional degrees of freedom that ultrasound introduces render the process more flexible, offering the potential to selectively promote the different processes of crystallization (nucleation, breakage, etc.). This technology is called sonocrystallization (SC) and has rapidly developed over the last 20 years. It has been reported that crystallization assisted by ultrasound leads to lower induction times and higher nucleation rates, improving crystal habit and crystal size distribution (CSD).[4−10] Furthermore, ultrasound can aid in inducing a specific polymorphic form.[11] A significant advantage offered by sonocrystallization is that seeding is no longer needed to induce primary nucleation, because sonication attains the same result more effectively and with better control.[12−14] This is particularly welcome in pharmaceutical processes. Ultrasound generators operate remotely and therefore are suitable for contained, sterile environments. Issues such as seeds choice and contamination are eliminated. Finally, the use of ultrasound is also expected to overcome problems associated with channel clogging and the pumping of suspensions. This has been demonstrated for the flow of particle suspensions in small-channel heat exchangers,

Received: May 6, 2016
Revised: July 8, 2016

DOI: 10.1021/acs.cgd.6b00696
Cryst. Growth Des. XXXX, XXX, XXX−XXX

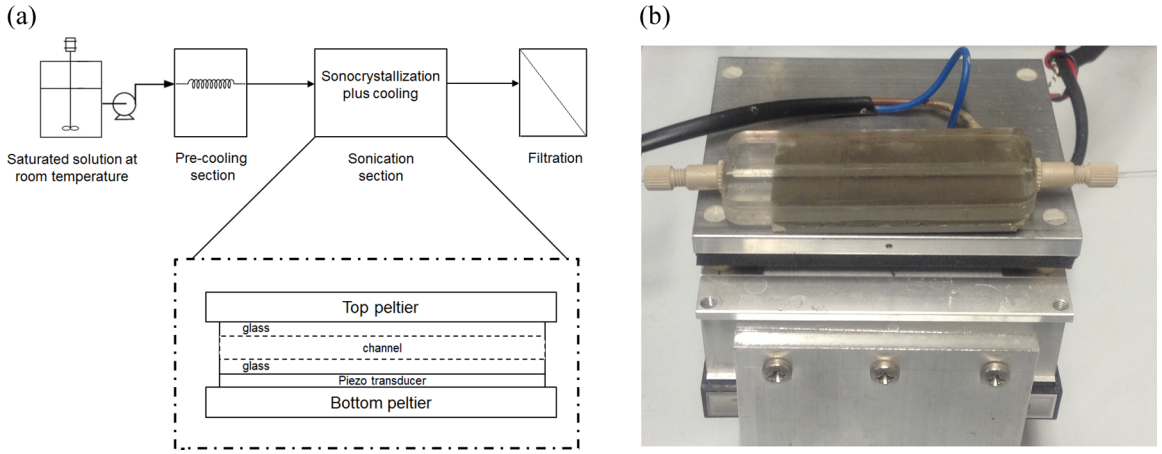

Figure 1. Experimental setup. (a) Schematic of the experimental setup. The crystallization/sonication unit is magnified for better clarity. The dimensions are not at scale. (b) Glass sonocrystallization unit equipped with a piezoelectric element on top of a Peltier element.

where fouling is drastically reduced in the presence of ultrasound.[15]

In large systems, process parameters such as temperature and concentration—crucial in cooling-driven crystallization—may not be uniform. This hinders batch-to-batch reproducibility. One of the most undesired consequences of the heterogeneous distribution of temperature and concentration within the crystallizer is the broad size distribution of the crystals.[1] For this reason, recently there has been an increased interest in the development of novel crystallization methods. In this regard, milli- and microfluidic devices offer great potential in delivering chemical compounds of higher quality. The benefits that they present have been widely reported in the literature:[16,17] milli and micro characteristic lengths lead to greater surface-to-volume ratios, intensifying mass and heat transfer, reducing temperature and concentration nonuniformities, and providing greater efficiency and control than those achievable in large crystallizers. To increase the production rates using these devices, scale-up by increasing the number of units instead of their size (numbering up) can be implemented. The past two decades have seen a remarkable progress in the development and fabrication of microfluidic systems for chemical and biological sciences.[18] Nowadays, milli- and microfluidics offer a wide range of new tools that can be employed in crystallization research, for screening of crystallization mechanisms as well as for investigating crystal nucleation kinetics.[19−22] Despite the various advantages presented, channel clogging is still an issue to be addressed when dealing with particles in narrow channels, because the synthesized particles or crystals tend to adhere to the channel walls blocking the system.[23,24]

In this work, we present a continuous millifluidic device equipped with a piezoelectric element as the ultrasound source to combine the advantages of continuous flow, ultrasound, and millifluidic technologies. Such a device helps us to better understand the sonocrystallization process. Piezoelectric elements are commonly used for particle separation in microchannels; see for instance Nilsson et al.[25] and Barnkob et al.[26] In those cases, however, depending on the size of the channel, which is on the order of a few hundred microns, the operating frequency of such transducers is on the order of MHz. It is widely reported in the literature that the probability of acoustic cavitation decreases by increasing the frequency.[27] In our design, since the use of ultrasound was to enhance crystal nucleation through acoustic cavitation, the operating frequency must be in the kHz range.[28] The hypothesis that acoustically activated bubbles are responsible for higher nucleation rates[29,30] was studied here by investigating the ultrasound parameters such as wave frequency and sonication time. In order to estimate the possibility of cavitation and its correspondence to sonocrystallization, the pressure field inside the capillary was calculated by means of numerical simulations. Thereafter, a cavitation threshold analysis was performed to investigate the cavitation of bubbles with a different size under the action of ultrasound. In this way, the modeling approach can be used as a design tool for identifying suitable operational ranges for the sonocrystallization unit.

This paper is organized as follows: in Section 2 the experimental setup and procedure are explained. The numerical approach to tackle the problem and the basic theory of the governing equations are summarized in Section 3. In Section 4 the results of the experiments and the simulations are described and discussed. Finally, in Section 5 a conclusion of the work and some suggestions for future work are presented.

EXPERIMENTAL SECTION

Chemicals. Adipic acid (hexanedioic acid, $(CH_2)_4(COOH)_2$ > 99.5% pure, Sigma-Aldrich, UK) was used as received without further purification, and solutions were made in deionized water (conductivity <0.2 μS/cm). The solubility of adipic acid in water at different temperatures was determined by fitting experimental data reported in the literature.[31,32] According to these data, a saturated solution at room temperature (22 °C) contains 2.12 g of adipic acid in 100 g of water. Moreover, the solubility concentration of adipic acid in water at lower temperatures can be derived from these data and used to determine the supersaturation ratio. The supersaturation ratio S is defined as the ratio between the actual concentration and the solubility concentration at a given temperature.

Experimental Setup and Procedure. Figure 1a shows a schematic of the sonocrystallization device. A saturated solution at room temperature (22 °C) was kept well mixed during the experiments by a magnetic stirrer. The solution was fed by a syringe pump (Mitos Duo XS-Pump, Dolomite, UK) to a precooling section. It flowed through polytetrafluoroethylene (PTFE) capillaries with I.D. = 1.55 mm and was cooled to 17 °C (the value required to create the desired supersaturation ratio, equal to S = 1.34) in a jacketed vessel whose temperature was controlled by a water bath (HAAKE F3, Germany). The temperature of the cooling liquid in the cooling jacket was controlled by a thermostat inside the water bath and also checked several times using a temperature probe. The flow rate of the solution

DOI: 10.1021/acs.cgd.6b00696
Cryst. Growth Des. XXXX, XXX, XXX−XXX

was kept constant at 2 mL/min in all experiments. Thus, the residence time of the solution in the precooling section (whose length was 50 cm) was approximately 28 s. The distance between the precooling section and the sonication section was kept as short as possible (ca. 5 cm) and insulated using glass wool and held in place with aluminum foil to mitigate heat transfer to the environment.

The sonocrystallization section comprised a glass chip with a straight channel and a flat piezoelectric element at the bottom. These were glued together by epoxy adhesive glue. The chip had dimensions of $W \times L \times H$ = 25 mm × 76 mm × 7 mm and was made of FOTURAN photo structurable glass (Mikroglas chemtech GmbH, Germany). The etched straight channel had dimensions of $W \times L \times H$ = 2 mm × 76 mm × 5 mm, and therefore the residence time of the solution in the channel was approximately 23 s. The vibration of the piezo in its thickness mode is important because the goal of this design is to create ultrasound waves inside the liquid perpendicularly to the channel axis. A channel height of 5 mm was chosen to allow enough space along the vertical direction for a quarter of a wavelength at lower frequencies and a few wavelengths at higher frequencies, ensuring that nodes and antinodes of the wave were present inside the channel. A channel width of 2 mm was chosen to avoid blockage of the channel. The inlet and outlet sections of the channel had square cross sections with dimensions of 2 mm × 2 mm. The change from a 2 mm × 2 mm section to a 2 mm × 5 mm one at the channel inlet and vice versa at the channel outlet helped to avoid extreme sudden width contractions and expansions at the inlet and outlet sections. PTFE tubes (I.D. = 1.55 mm) were connected to the channel inlet and outlet on the chip with IDEX NanoPort connectors that were glued using epoxy resin. The piezoelectric element was made of lead zirconate titanate (PZT-5A) and had dimensions of $W \times L \times H$ = 36.2 mm × 72.4 mm × 1 mm (Piezo Systems, Inc., USA). To keep the temperature uniform inside the channel, and to control the supersaturation of the solution, the chip surfaces were cooled with Peltier elements mounted at the bottom and top of the sonocrystallization unit. Figure 1b shows the glass chip with the piezoelectric element on top of one of the Peltier elements. To verify temperature uniformity, the temperature along the channel with the flowing solution was measured using a thermocouple inserted inside the channel. A difference of 0.4 °C was observed between the entrance and exit sections of the channel.

Sinusoidal waves were generated using a signal generator (33210A Function/Arbitrary Waveform Generator, Agilent Technologies, Inc., USA) and amplified using a power amplifier (1020L, Electronics & Innovation, Inc., USA) to excite the piezoelectric element. We used conductive epoxy glue (Chemotronics, USA) which contains silver for connecting the electrical wires to the surfaces of the piezo. Before gluing the wires to the surface of the piezo, we painted its surface with silver paint conductive adhesive (RS Components Ltd., UK) which filled the crevices on the surface (if any) with silver, therefore improving the electrical connection. Since the conversion from electrical power to acoustic power is not ideal, a part of the power is converted into heat. Furthermore, transmission of high power levels to the piezoelectric element affects the electrical connection points, and, after a while, the wires tend to detach from the surface of the piezo. Both issues become significant if the piezoelectric element works continuously. To mitigate them, ultrasound was applied in burst mode. Using bursts, we could apply ultrasound in an ON/OFF mode during a fixed time interval. In our experiments, we fixed this time interval at two seconds. The ratio between the ON period and the interval of two seconds is called duty cycle. So, for instance, at an arbitrary frequency ν, if the number of ON ultrasound cycles is n, then ultrasound is applied to the system for n/ν seconds and the rest of the time, i.e., $2 - n/\nu$ seconds, the system is silent (OFF). The duty cycle is then equal to $n/(2\nu)$. Using this ON/OFF mode, the power amplitude could be increased without heating up the system and detaching the electrical connections.

The conversion of electrical power to heat is significant if the electrical circuit does not work in its optimum operating condition; this happens when the impedances of the load and the source are not matched, and consequently a small portion of the electrical power is converted to ultrasound power. The optimum operating condition is achieved when the system works at one of its electrical resonance frequencies. To find the latter, we swept the frequency of the input signal over a wide range within the ultrasonic regime (>20 kHz). Before crystallization experiments, the piezoelectric element was excited continuously, and the input and reflected powers were read by the amplifier. Whenever the reflected power to the amplifier vanished, the system was working at one of its electrical resonance frequencies. We found four resonance frequencies: 42 kHz, 224 kHz, 660 kHz, and 1.09 MHz and used these values in carrying out the parametric study of the effect of frequency on sonocrystallization in our system.

The solution exiting the channel was collected on Whatman cellulose nitrate membrane filter papers (Fisher Scientific Ltd., UK) with an average pore size of 0.45 μm. To avoid the accumulation of the solution containing suspended crystals on the filter paper and the subsequent growth of the crystals, vacuum filtration was used. The filter paper was then dried for 10 min on a hot plate at 80 °C. By measuring the weight of the filter paper before and after the experiment (when crystals were collected on it), we could calculate the production rate of the crystals. Thereafter, the collected crystals were suspended in vegetable oil, in which adipic acid is insoluble, and homogeneously dispersed using an ultrasonic water bath (Branson 2510E-MT, 42 kHz, 100 W) for 20 min. This slurry was analyzed using a laser diffraction particle size analyzer (LS 13320 Beckman Coulter, UK) to determine the CSD. To check the reproducibility of the experiments, each experiment was repeated three times and the CSDs were measured. We ensured that the ultrasonic water bath did not cause primary particles break up. This could be proven by comparing the CSD of the raw adipic acid crystals purchased, which did not contain agglomerates, and the CSD of the same crystals after having treated them in the ultrasonic water bath according to our protocol. The comparison showed that the two CSDs were nearly identical, and therefore this experiment confirmed that in the deagglomeration stage the primary crystals produced by ultrasound did not break up in the ultrasonic bath.

■ MODELING OF THE WAVE PROPAGATION

This section explains the modeling and numerical simulation approach adopted to investigate the acoustic pressure distribution inside the millichannel. The goal was to shed light on the effects of ultrasound on sonocrystallization. In the model, the loss of electrical power in the piezoelectric element, the attenuation of the ultrasound wave in the bubbly liquid, and a threshold criterion for the prediction of transient bubble cavitation were considered. The numerical simulations accounted for the spatial distribution of pressure waves in the liquid to investigate the probability of transient cavitation in different spatial locations using the threshold criterion just mentioned. In modeling the effect of bubbles on wave attenuation, bubbles were assumed to be distributed over the size. Considering a distribution for the cavitation bubbles allows modeling the wave propagation within the system in detail and determining the type of cavitation (stable or transient) for a range of bubble nuclei. This permits identifying more accurately (compared to the case where a single size for all the bubble nuclei is assumed) how probable transient cavitation is in each point of the crystallizer. The transient cavitation activity spatial profile in the system relates to the nucleation rate spatial profile (the rate is higher in the locations where the number of transient cavitation events is larger), which in turn affects the crystal size distribution.

To avoid misunderstandings, one clarification is in order. In classifying the cavitation type, different terminologies have been used in the literature. In a sound field, depending on the initial radius of a bubble and on the frequency and pressure amplitude of the ultrasonic wave, a bubble may collapse violently in one acoustic cycle (case 1), may oscillate in a strong nonlinear way

DOI: 10.1021/acs.cgd.6b00696
Cryst. Growth Des. XXXX, XXX, XXX−XXX

with slow expansions and rapid contractions (case 2), or may oscillate around its equilibrium radius nonlinearly and with small oscillation amplitudes compared to its radius (case 3). In case 1, the bubble fragments into daughter bubbles at the end of a single acoustic cycle, following a strong collapse which generates shock waves, microjets, and hot spots with high local pressures and temperatures. In case 2, the bubble does not break into daughter bubbles. Over one cycle, it grows in the rarefaction phase, then collapses in the compression phase reaching a minimum radius smaller than its equilibrium radius, and finally oscillates about this radius various times. This pattern repeats itself over several cycles. In case 3, the bubble oscillates for long periods (orders of magnitude larger than the period of the ultrasonic wave) and is stabilized by the diffusion of gas through its interface.

In the literature, some authors (e.g., in refs 33−35) refer to case 1 as *inertial* or *transient cavitation* and to cases 2 and 3 as *stable cavitation*. Other authors (e.g., in refs 36−38), on the other hand, refer to cases 1 and 2 as *transient cavitation* and to case 3 as *stable cavitation*. In this paper, the second terminology is adopted.

Theory. The propagation of small amplitude pressure waves in a fluid medium is governed by the following homogeneous wave equation

$$\partial_{tt}^2 p + c^2 \nabla^2 p = 0 \tag{1}$$

Here p is the pressure and c is the speed of sound in the medium. The pressure can be decomposed into a spatially varying amplitude and a harmonic contribution as

$$p(\mathbf{r}, t) = \frac{1}{2}[P(\mathbf{r})e^{i\omega t} + \overline{P}(\mathbf{r})\mathrm{e}^{-i\omega t}] \tag{2}$$

where ω is the angular frequency of the wave and the overline denotes the complex conjugate. By substituting eq 2 in eq 1, the time independent wave equation in the frequency domain, which is a Helmholtz-type equation, is obtained

$$\nabla^2 P + k^2 P = 0 \tag{3}$$

In this equation, $k \equiv \omega/c$ denotes the wavenumber. This equation must be solved for the glass layers as well as for the liquid phase (water) containing bubbles inside the channel.

The ultrasound wave attenuates significantly because of the cavitation bubbles present in the liquid. To consider the attenuation of the wave in the bubbly medium, the linearized model proposed by Prosperetti[39] and Commander and Prosperetti[40] was selected. In this model, the wavenumber in the Helmholtz equation is written as a complex number whose imaginary part relates to the damping effect of the bubbles. The modified wave equation reads

$$\nabla^2 P + k_m^2 P = 0 \tag{4}$$

The complex wavenumber, k_m, is given by

$$k_m^2 = \frac{\omega^2}{c^2} + 4\pi\omega^2 \int_0^\infty \frac{R_0 f(R_0, \mathbf{r})}{\omega_0^2 - \omega^2 + 2ib\omega}\, \mathrm{d}R_0 \tag{5}$$

In this equation, $f(R_0, \mathbf{r})$ is the number density function (NDF) of the bubble population. This function describes how the bubbles are distributed over the size coordinate R_0 at every spatial location $\mathbf{r}$ in the millichannel. In particular, by definition, the expected number of bubbles per unit volume with size in the range $\mathrm{d}R_0$ around R_0 at position $\mathbf{r}$ in space is equal to

$$\mathrm{d}N = f(R_0, \mathbf{r})\, \mathrm{d}R_0 \tag{6}$$

In eq 5, ω_0 represents the resonance frequency of the bubbles, defined as

$$\omega_0^2 \equiv \frac{p_0}{\rho R_0^2}\left[\Re(\Phi) - \frac{2\sigma}{R_0 p_0}\right] \tag{7}$$

Here p_0 is the undisturbed pressure in the bubble position, which is higher than the equilibrium pressure p_∞ in the liquid by the amount $2\sigma/R_0$ due to the surface tension σ. The complex dimensionless parameter Φ is defined as

$$\Phi \equiv \frac{3\gamma}{1 - 3(\gamma - 1)i\chi[(i/\chi)^{1/2}\coth(i/\chi)^{1/2} - 1]} \tag{8}$$

In this expression, γ is the specific heat ratio of the gas inside the bubble and the dimensionless parameter χ is defined as

$$\chi \equiv \frac{D}{\omega R_0^2} \tag{9}$$

where D is the thermal diffusivity of the gas. The damping factor b in eq 5 is defined as

$$b \equiv \frac{2\mu}{\rho R_0^2} + \frac{p_0}{2\rho\omega R_0^2}\Im(\Phi) + \frac{\omega^2 R_0}{2c} \tag{10}$$

where μ denotes the viscosity of the medium.

As one can see from eq 5, to calculate k_m we require the distribution of bubble nuclei in the liquid. This should be assumed. The integral of the NDF over the whole span of possible bubble radii gives the total number of bubbles per unit volume in the liquid. This number is very hard to measure. On the other hand, the volume fraction of bubbles β, which is the ratio of the volume occupied by the gas phase to the total volume, is a measurable quantity.[41,42] Assuming that bubbles are spherical, we can write the volume fraction as

$$\beta = \frac{4\pi}{3}\int_0^\infty R_0^3 f(R_0, \mathbf{r})\, \mathrm{d}R_0 \tag{11}$$

By assuming a reasonable value for β and a reasonable functional form for the NDF, the value of k_m can be calculated using numerical integration. To solve the Helmholtz equation, a typical value of $\beta = 3 \times 10^{-4}$ was selected[40,41,43] and was assumed to be spatially uniform. Moreover, a Gaussian distribution of initial nuclei size, also uniformly distributed in space [$f = f(R_0)$], compatible with experimental observations was assumed.[44] In their experiment, Mettin et al.[44] analyzed the time dependent radii of the bubbles by image processing. Thereafter, by measuring the pressure amplitude at bubble positions, they calculated the initial nuclei size of the bubbles. According to their results, the NDF can be approximated by the following distribution

$$f(R_0) = \begin{cases} Ce^{(R_0 - \mathrm{SD_G})^2/R_G^2}, & R_{\min} \le R_0 \le R_{\max}; \\ 0, & \text{otherwise} \end{cases} \tag{12}$$

We adopted this NDF for our modeling, and, following Mettin et al.,[44] we considered the radii of the bubbles in a range from $R_{\min} = 1$ μm to $R_{\max} = 10$ μm, setting $R_G = 2$ μm and $\mathrm{SD_G} = 5$ μm. The constant C was computed in such a way as to match the volume fraction of the bubbles based on eq 11. The initial bubble nuclei distribution is shown in Figure 2.

DOI: 10.1021/acs.cgd.6b00696
Cryst. Growth Des. XXXX, XXX, XXX−XXX

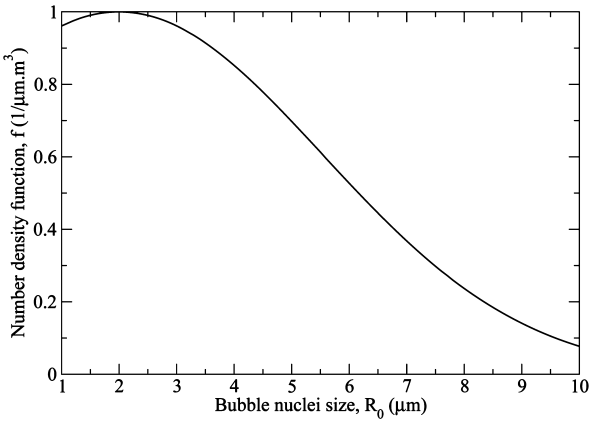

Figure 2. Initial size distribution for bubble nuclei.

The mean size R_{mean} and the standard deviation SD of the bubble size distribution reported in eq 12 are given by the following relations:

$$R_{mean} = \frac{\int_1^{10} R_0 f(R_0)\, dR_0}{\int_1^{10} f(R_0)\, dR_0}$$
$$SD^2 = \frac{\int_1^{10} (R_0 - R_{mean})^2 f(R_0)\, dR_0}{\int_1^{10} f(R_0)\, dR_0} \quad (13)$$

Note that these values differ from those of R_G and SD_G, which are the mean and the standard deviation of the Gaussian distribution (the latter coincides with the bubble size distribution only in the radius range between 1 and 10 μm). In particular, from numerical integration, one finds that R_{mean} = 3.74 μm and SD = 1.99 μm.

Once k_m is obtained, eq 4 can be solved numerically. In this paper, the numerical simulation was performed using the finite element method (FEM). To do this, the wave equation without attenuation (eq 3) for the glass layer and eq 4, which includes the attenuating effect of the bubbles, for the liquid inside the channel were solved simultaneously using COMSOL Multiphysics software. The remaining physical properties required for the simulations are indicated in Table 1.

Geometry, Boundary Conditions, and Numerical Method. The geometry of the crystallization unit is shown in Figure 3. The piezoelectric element had dimensions $W \times L \times H$ = 36.2 mm × 72.4 mm × 1 mm. The glass layer was a $W \times L \times H$ = 25 mm × 76 mm × 7 mm rectangular parallelepiped in which a channel with the dimensions of $W \times L \times H$ = 2 mm × 76 mm × 5 mm was formed.

The piezoelectric element was made of lead zirconate titanate (PZT-5A) whose properties were predefined in the software. The theory of converting electrical power to mechanical vibration and its numerical implementation are developed elsewhere and are not repeated here.[46−49] In the "acoustic-piezoelectric interaction" module of the software, the electrical potential (voltage) was set as the input for excitation of the piezo structure. To estimate this value for the simulations, we required the value of electrical potential set in the experiments as well as the efficiency of the piezo. In the experiments, the input voltage set in the signal generator was amplified using the amplifier whose gain was provided by a calibration curve by the supplier. According to this calibration curve, for an input value of 400 mV_{pp}, the output rms voltage of the amplifier was calculated as 65.5 V. To calculate the total electromechanical efficiency of the piezo, the following equation was used, which assumed a quasi-static operation of the transducer

$$\eta = 1 - \frac{\tan \delta}{k_{em}^2 Q_m} \quad (14)$$

where $\tan \delta$ is the dielectric loss or dissipation factor, k_{em} is the electromechanical coupling factor, and Q_m is the mechanical damping factor of the piezo. The electromechanical efficiency of the piezo, based on properties provided by the supplier, was calculated as 79.6%, and therefore the input electrical potential between the bottom and top surfaces of the piezo in the model was set to V = 0.796 × 65.5 = 52.2 V. For the vibration of the transducer, the bottom surface, which was in contact with the bottom Peltier element, was assumed to be fixed, and the top surface was free to vibrate.

The acoustic pressure wave in glass, and consequently in water, was induced by the vibration of the piezoelectric element; these vibrations generated mechanical stress in the latter. The boundary condition to be set at the interface between the top surface of the piezo and the glass layer was therefore the equality of the normal component of the structural acceleration (the second derivative of the structural displacement with respect to time) of the piezo at the interface and the normal component of the pressure gradient in the glass, i.e.,

$$\mathbf{n} \cdot \left(\frac{\nabla P}{\rho_g} \right) = -\mathbf{n} \cdot \partial_{tt}^2 \mathbf{u} \quad (15)$$

and the equality of the normal component of the stress tensor and the pressure load (force per unit area) amplitude induced in the glass, i.e.,

$$\mathbf{nn} : \boldsymbol{\tau} = P \quad (16)$$

In these equations, $\mathbf{n}$ is the outward-pointing unit normal vector to a surface, $\boldsymbol{u}$ is the displacement vector at the interface, and $\boldsymbol{\tau}$ is the stress tensor. For the interface between the glass layer and the water inside the channel, the second condition (eq 16) was modified by equating the acoustic pressure amplitude in the glass and in the water at the interface.

All side walls of the glass unit were in contact with air. These were assumed to be pressure release boundaries and were modeled with a Dirichlet-type boundary condition setting P = 0. The top wall was fixed with the top Peltier element and was modeled as a rigid reflecting wall using a Neumann type boundary condition, i.e., $\partial_n P$ = 0.

Unstructured tetrahedral meshing was used for discretization of the geometry. The number of cells should increase as the

Table 1. Physical Properties Applied in the Simulations[a]

γ	D (m^2/s)	σ (N/m)	ρ (kg/m^3)	c (m/s)	ρ_g (kg/m^3)	c_g (m/s)	p_0 (Pa)
1.4	1.9×10^{-5}	0.0725	998	1480	2230	5647	101325

[a]Subscript "g" stands for glass.

DOI: 10.1021/acs.cgd.6b00696
Cryst. Growth Des. XXXX, XXX, XXX−XXX

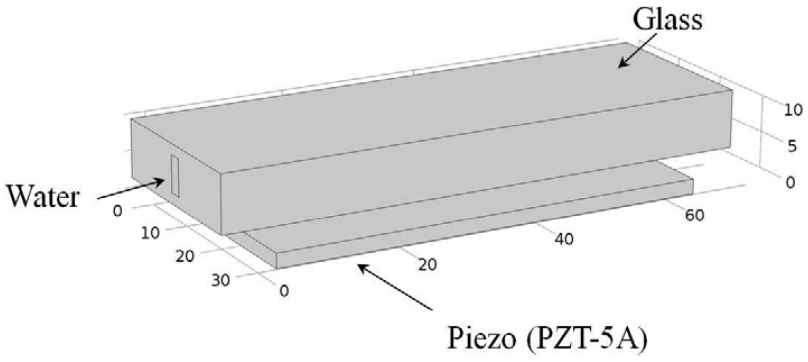

Figure 3. Geometry of the crystallization millifluidic chip.

frequency increases to avoid pollution effects in the finite element analysis of the Helmholtz equation.[50−52] Therefore, the size of the elements was selected to satisfy the following condition:

$$k \cdot h < 1 \tag{17}$$

where h is the average size of the element. Since the wavenumber is different in glass and water, the element size should be selected in a way to satisfy the condition in both materials. Table 2 shows the criteria for the size of elements and the number of selected degrees of freedoms (DOFs) for the simulations at different frequencies. The simulation time on a 64-bit Windows operating system and Intel Core i5-3470 CPU at 3.2 GHz speed and 8.0 GB RAM varied from approximately 5 min for the case of 42 kHz to about 1 h for the case of 1090 kHz.

Table 2. Maximum Allowable Cell Size at Different Frequencies and the Number of Selected DOFs for the Simulations

ν (kHz)	$h_{max,w}$ (mm)	$h_{max,g}$ (mm)	DOFs
42	5.60	21.40	211796
224	1.05	4.00	466466
660	0.36	1.36	546969
1090	0.22	0.82	588824

The last part of the model deals with the probability of transient cavitation in the liquid. This analysis was conducted using the transient cavitation threshold proposed by Apfel[53] and Neppiras,[37] which compares the shrinkage velocity of the bubble wall during its collapse ($\dot{R}$) with the speed of sound c. If the ratio of the two speeds, $\dot{R}/c$, which is usually known as acoustic Mach number (Ma), exceeds unity, the cavitation of the bubble is assumed to be transient. To find the value of $\dot{R}$, the radial dynamics of the bubbles must be solved using a Rayleigh−Plesset type of equation. Here, we selected the Keller−Miksis equation.[54] This equation reads:

$$\rho\left[\left(1-\frac{\dot{R}}{c}\right)R\ddot{R}+\frac{3}{2}\dot{R}^2\left(1-\frac{\dot{R}}{3c}\right)\right] = \left(1+\frac{\dot{R}}{c}+\frac{R}{c}\frac{\mathrm{d}}{\mathrm{d}t}\right)\left(p_{gas}-\frac{2\sigma}{R}-\frac{4\mu\dot{R}}{R}-p\right) \tag{18}$$

in which overdots denote differentiation with respect to time, and p is the pressure in the liquid at the bubble center in the presence of a sound field $p = p_0 - P\sin(\omega t)$. To solve this equation, we required the initial size for the bubble nuclei R_0 (initial condition to be set at time $t = 0$) and the acoustic pressure amplitude P. We selected a hundred initial nuclei sizes in the range from $R_{min} = 1$ μm to $R_{max} = 10$ μm, the range in which the NDF is non-negligible, with increments of $\Delta R_0 = 0.1$ μm. The acoustic pressure amplitude was obtained from the numerical simulation of the wave equation at different positions inside the channel as a spatial distribution. The maximum value obtained for the acoustic pressure was 1.3 MPa at $\nu = 42$ kHz. We selected this value as the maximum possible magnitude for P in eq 18, for any frequency (not just for 42 kHz) in order to compare the results in the same pressure amplitude range. We divided the pressure amplitude range from 0 to 1.3 MPa, with $\Delta P = 5$ kPa increments and solved eq 18 at the given frequency for all the possible R_0, P combinations. By doing this analysis, we generated four contour maps (one for each resonance frequency) for the magnitude of $\dot{R}/c$ in the R_0, P plane (see Figure 8, which we will discuss later on). The probability of transient cavitation at different frequencies can be investigated inside the channel by using these contour maps. This analysis helps us to correlate the transient cavitation with the enhancement of sonocrystallization.

RESULTS AND DISCUSSION

To better understand the correspondence between transient cavitation and crystallization and to interpret and discuss the results obtained experimentally, we present the results of the modeling analysis prior to the experimental observations. The simulation results presented in this part helps us to understand how probable transient cavitation is at different operating conditions of the system.

Numerical Simulation Results and Cavitation Threshold Analysis. The imaginary part of k_m, the "attenuation coefficient", which represents the damping effect of bubbles on the pressure wave, is plotted in Figure 4 as a function of the wave frequency. It can be seen that the damping effect of bubbles can be significant even at the low value of $\beta = 3 \times 10^{-4}$ assumed for the bubble population. This effect is even more considerable at the higher frequencies selected in this study (the curve peaks in the MHz range). However, the attenuation decreases again at very high frequencies. The reason for the presence of a peak in the attenuation curve is due to the strong dependence of the viscous, thermal, and acoustic damping on the wave frequency. For further details, the interested reader is referred to refs 39, 40, 43, and 55−59. The corresponding value of the attenuation coefficient at each frequency was calculated from this curve and implemented in the numerical simulations.

Results for the distribution of the pressure amplitude over two cross sections passing through the middle of the channel,

DOI: 10.1021/acs.cgd.6b00696
Cryst. Growth Des. XXXX, XXX, XXX−XXX

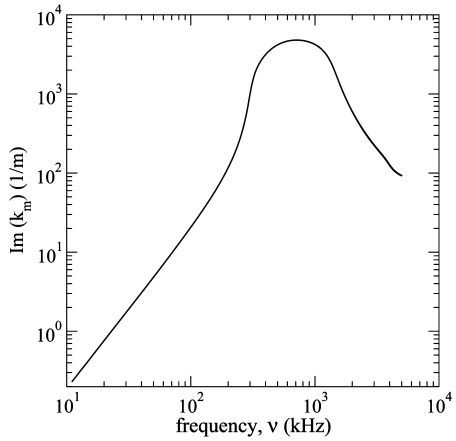

Figure 4. Attenuation of the ultrasound wave due to the damping effect of bubbles vs frequency.

one vertical and one horizontal, for four different frequencies are shown in Figures 5 and 6. The pressure amplitude distributions are different at different frequencies, both in terms of value and pattern. At 42 kHz, the pressure amplitude is almost uniform inside the channel. Apart from the two small sections at the inlet and outlet of the channel, which are close to pressure release boundaries, the pressure amplitude is quite high over the whole cross section. More specifically, its amplitude exceeds 1 MPa at the central part of the channel; this value is sufficiently large to create transient cavitation, as will be illustrated later in the cavitation threshold analysis. Although the pressure amplitude decreases by increasing the distance from the surface of the piezo, its value remains high enough to have transient cavitation at the top of the channel, according to the cavitation threshold analysis which will be explained later (see Figure 8a). In contrast, at 224 kHz some localized high pressure zones, with amplitudes of about 0.4 MPa, are present inside the channel. However, in this case the pressure amplitude distribution is highly nonuniform, with regions, even close to the surface of the piezo, where the pressure amplitude is quite low and insufficient to generate transient cavitation bubbles, as we will see later in the section on the cavitation threshold analysis (see Figure 8b).

The pressure distribution at higher frequencies, namely, 660 kHz and 1090 kHz, is quite different from the lower frequencies of 42 kHz and 224 kHz. Since the attenuation coefficient due to the presence of the bubbles is very high at these frequencies, the pressure wave damps quickly inside the channel. The pressure amplitude does not exceed 0.2 MPa for the frequency of 660 kHz, and this value is present only in a small region close to the piezo surface at the bottom of the channel. At 1090 kHz, the maximum amplitude does not even reach 0.05 MPa. These amplitudes are not sufficient to collapse bubbles and generate transient cavitation inside the liquid medium, as we will see later in the section on the cavitation threshold analysis (see Figure 8d).

The pressure amplitude along the axis of the channel from inlet to outlet is shown in Figure 7, in order to clarify the effect of frequency on pressure variation. It can be seen that there are many more fluctuations at higher frequencies. This is because at higher frequencies the wavelength decreases, and therefore, since the channel has constant length, more nodes and antinodes of the wave are present along the channel. This results in a larger number of fluctuations. If the outcome of higher acoustic pressure (such as transient cavitation) is required at high frequencies, the input power to the system should increase drastically. On the other hand, working at lower frequencies increases the probability of transient cavitation which is desirable for crystallization.[29,37,60]

The results of the cavitation threshold analysis are shown in Figure 8, where the contour maps of the logarithm of the acoustic Mach number is plotted for each frequency in the R_0, P plane. For clarity, the isoline of Ma = 1, above which the cavitation is assumed to be transient, is shown in bold. Moreover, the region in which the sonocrystallization device is most likely to operate (the possible R_0, P combinations) is shown as a hashed area in each plot. The range of bubble radius selected to plot the hashed areas is based on the most expected size values from the NDF, i.e., from R_{mean} − SD = 1.75 μm to R_{mean} + SD = 5.73 μm. The upper limit for the pressure amplitudes, which is considered for the hashed areas is the maximum pressure amplitude obtained from COMSOL simulations at each frequency (Figures 5 and 6). The area of overlap between the operating conditions (hashed area) and

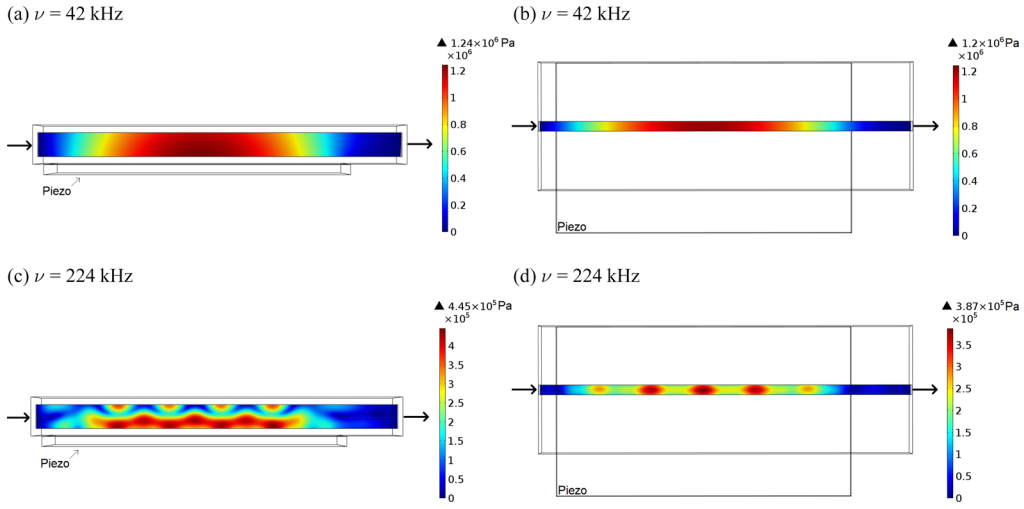

Figure 5. Pressure amplitude maps in the middle cross sections of the channel for two lower frequencies. Panels a and c, side view on the vertical cross-section and b and d, top view on the horizontal cross section. The flow direction is from left to right.

DOI: 10.1021/acs.cgd.6b00696
Cryst. Growth Des. XXXX, XXX, XXX−XXX

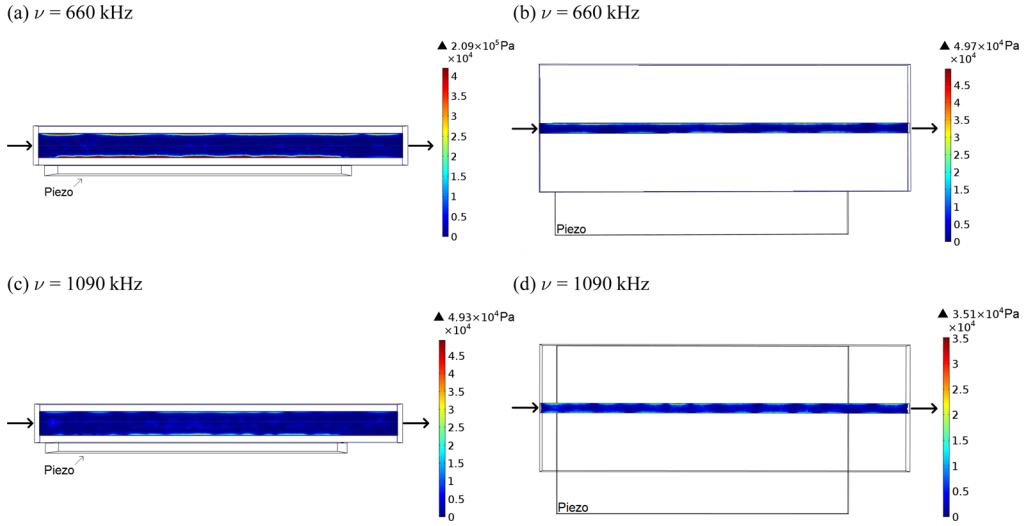

Figure 6. Pressure amplitude maps in the middle cross sections of the channel for two higher frequencies. Panels a and c, side view on the vertical cross section and b and d, top view on the horizontal cross section. The flow direction is from left to right.

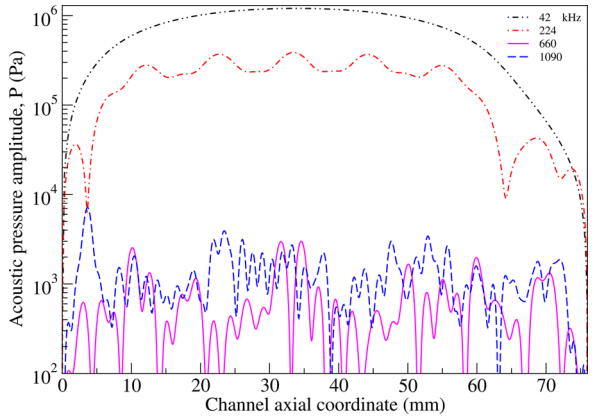

Figure 7. Variation of pressure amplitude along the axis of the channel from inlet to outlet at different frequencies.

the region above the isoline Ma = 1 can be used as a criterion for the likelihood of transient cavitation. This area is reduced when the frequency is increased from 42 kHz to 224 kHz and vanishes at the other two higher frequencies. At 42 kHz, transient cavitation is expected for all assumed bubble sizes. Since a big part of the channel experiences high pressure amplitude (Figure 5a,b), one expects sufficient transient cavitation activity at this frequency. At 224 kHz, the area of likely transient cavitation is smaller compared to the case of 42 kHz. All assumed bubble sizes can experience pressure amplitudes which can lead them to undergo transient cavitation. The pressure amplitude range is narrower than that at 42 kHz (this results in weaker collapse of bubbles), and furthermore the regions inside the channel where these amplitudes are present (Figure 5c,d) are smaller compared to the high pressure zones in the case of 42 kHz. Therefore, we can expect less transient cavitation activity at this frequency. At 660 kHz and 1090 kHz, the area in which transient cavitation is probable vanishes in the contour maps. This shows that the transient cavitation of bubbles in the assumed size range using our setup is unlikely.

Since transient cavitation of bubbles is believed to be the most significant phenomenon in the enhancement of sonocrystallization,[29−31] one can conclude from this analysis that the consequences of transient cavitation, such as higher nucleation rates of crystals, are less likely at higher frequencies. Thus, at higher frequencies one can expect bigger mean crystal sizes. This is because, at lower nucleation rates, fewer crystals generate; these crystals can thus grow to a larger size. This was observed in our experiments, whose results are presented in the next section.

Crystal Size Distribution and Morphology. As expected from the results of the modeling section, higher nucleation rates are less likely at higher frequencies due to less transient cavitation activity. This results in larger mean crystal sizes, as our experiments confirm. Figure 9 shows the effect of wave frequency on the CDS for the same frequencies considered in the modeling section, except for 1090 kHz. In the experiments at 1090 kHz, not enough crystals formed for analysis. The reason, as predicted by the model, is the very low probability of transient cavitation activity at this frequency. To have a reasonable comparison of the CSDs at different frequencies, the ultrasound duty cycle for all the cases was fixed at 1.19%. To achieve this, the number of ultrasound cycles for each frequency had to be changed. The duty cycle of 1.19% corresponds to 1000 cycles at 42 kHz, 5333 cycles at 224 kHz, and 15714 cycles at 660 kHz. As one can see from Figure 9, the mean crystal size increases from approximately 32 μm at 42 kHz to approximately 40 μm at 660 kHz (each experiment was repeated three times; the standard deviation of the experimental values obtained for the mean size was equal to 2.6 μm at 42 kHz, 2.0 μm at 224 kHz, and 0.4 μm at 660 kHz). This outcome was expected in the light of the analysis carried out using the model. Transient cavitation of large bubbles is more favorable at lower frequencies, and its probability decreases when the frequency rises.[27] So, it is concluded that crystal nucleation is less enhanced at higher frequencies (even at increased numbers of ultrasound cycles, which are necessary to yield the same sonication time) because of weaker transient cavitation activity. Figure 9 shows that also the standard deviation (SD) and the coefficient of variation (CV), which is the ratio between the standard deviation and the mean crystal size, of the CSD increase when the frequency rises. The distribution, therefore, becomes broader. In the considerations above, we assumed that crystal breakage is absent. This assumption was investigated experimentally.

DOI: 10.1021/acs.cgd.6b00696
Cryst. Growth Des. XXXX, XXX, XXX−XXX

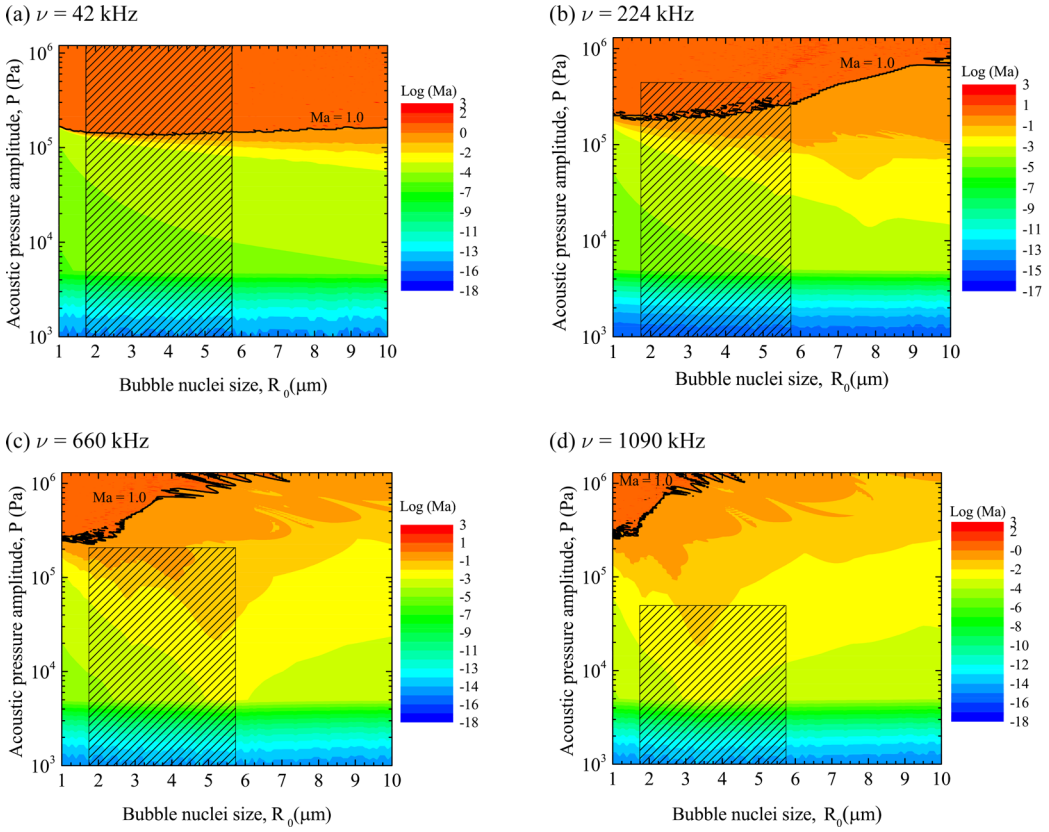

Figure 8. Contour of the logarithm of acoustic Mach number Ma in the R_0, P plane at different frequencies (a: 42 kHz, b: 224 kHz, c: 660 kHz, d: 1090 kHz). The cavitation threshold above which the set of parameters results in transient collapse of bubbles is defined as Ma > 1. The zone of probable transient cavitation is the region above the isoline of Ma = 1 (solid thick line) in each figure. The hashed area in each contour represents the region in which the chip utilized in this work is most likely to operate. The overlap of the transient cavitation threshold and the hashed area is an index of probability of transient cavitation occurring in the chip.

To investigate whether ultrasound causes breakage of crystals in our system, we conducted experiments where we ground purchased raw crystals and used them as seed crystals. The mean size of the sieved and ground crystals used for the breakage experiments was ca. 40 μm. Breakage is size dependent; nevertheless, the bigger the crystals are, the more they are prone to break. In the experiments conducted to study the effects of duty cycle and frequency on crystallization, the mean size of the crystals never exceeded 40 μm. So, it can be concluded that, if breakage did not take place in the breakage experiments (where larger crystals were present), it should not take place in the other experiments (where smaller crystals were present).

We suspended the seed crystals in a saturated solution at room temperature, and we passed the solution through the device, collecting the crystals at the exit on filter papers. We ran this experiment in two extreme conditions, namely, without applying ultrasound and at maximum duty cycle (7.15%) at the lowest frequency, i.e., ν = 42 kHz. We believe that if at this condition (lowest frequency and maximum duty cycle) the system does not cause crystal breakage, then the latter is very unlikely at the other operating conditions. This is because crystal breakage, when it takes place, is enhanced by transient cavitation of bubbles. The latter, as seen, is more favorable at lower frequencies. Moreover, the number of transient cavitation events increases when the duty cycle (and therefore the sonication time) increases. As a consequence, if at the lowest frequency and maximum duty cycle crystal breakage is not observed, it is expected that the same should happen at higher frequencies and lower duty cycles. We repeated each experiment three times and measured the CSDs, which are shown in Figure 10. The mean size of the crystals in both cases are almost identical and approximately 42 μm. From this result, we propose the hypothesis that, in this system, ultrasound enhances crystal nucleation but does not cause crystal breakage.

Figure 11 shows pictures of the adipic acid crystals collected after the breakage experiments. In silent conditions, adipic acid normally crystallizes from aqueous solutions as flat, slightly elongated, hexagonal, monoclinic plates.[61] This characteristic crystalline structure changes when we grind crystals for the breakage experiments. Crystals become more irregular and rounded, and the typical hexagonal-like habit is lost (Figure 11a). If breakage occurred in the presence of ultrasound, the mean size of these crystals should decrease and their shape should become more irregular. However, as it can be seen in Figure 11b, it is difficult to appreciate any difference in crystal morphology between the two figures, since the shape of the crystals as well as their surface roughness are not altered by ultrasound. This analysis further indicates that ultrasound promotes nucleation but does not induce breakage of crystals in this sonocrystallization device.

To investigate the effect of ultrasound bursts on the final product, different levels of ultrasound duty cycle were applied at a constant frequency of 42 kHz and a voltage amplitude of 400 mV_{pp}.

DOI: 10.1021/acs.cgd.6b00696
Cryst. Growth Des. XXXX, XXX, XXX−XXX

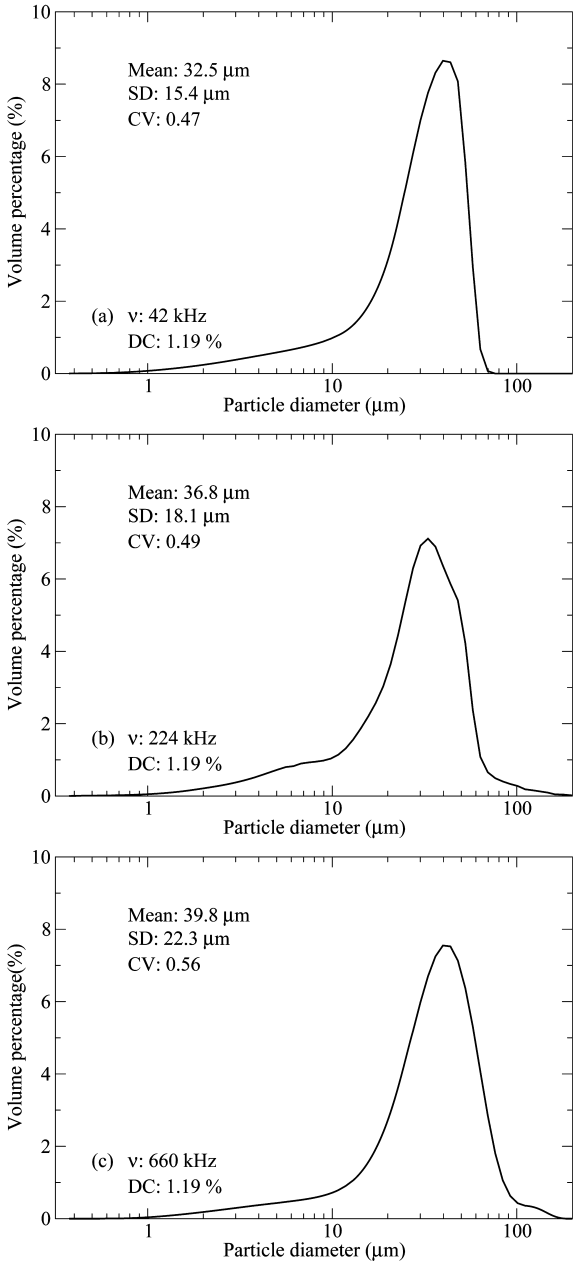

Figure 9. Crystal size distributions at the duty cycle of 1.19% at different frequencies (a: 42 kHz, b: 224 kHz, and c: 660 kHz). S = 1.34. Amplitude = 400 mV_{pp}.

Figure 12 shows the averaged CSD of three experiments for four values of duty cycle, namely, 0.6, 2.38, 4.76, and 7.15%. These numbers correspond to 500, 2000, 4000, and 6000 ultrasound cycles over the two-second time interval, respectively. The values of the mean size of crystals, the standard deviation of the distributions, and the coefficient of variation are reported. The mean crystal size decreases gradually from ca. 35 μm at duty cycle of 0.6% to approximately 25 μm at duty cycle of 7.15% (the standard deviation of the experimental values obtained for the mean size was equal to 0.9 μm at a duty cycle of 0.6%, 1.7 μm at a duty cycle of 2.38%, 0.8 μm at a duty cycle of 4.76%, and 1.8 μm at a duty cycle of 7.15%). The values of the mean size obtained are smaller than those found in larger-scale continuous sonocrystallization setups. For instance, Narducci et al.[62] used a mixed-suspension,

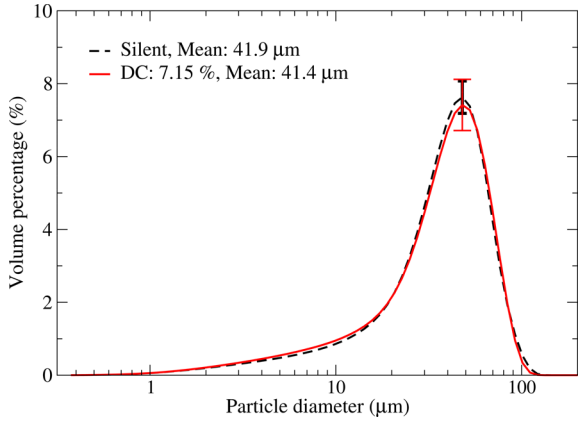

Figure 10. Crystal size distributions in silent and sonicated conditions. S = 1.34. ν = 42 kHz. Amplitude = 400 mV_{pp}.

mixed-product-removal (MSMPR) sonocrystallizer as a continuous system for crystallization of adipic acid equipped with an ultrasonic horn and obtained a mean size of approximately 65 μm. The reason for the smaller mean crystal size produced by our chip is the considerably lower residence time (23 s in our system, 10 min in that investigated by Narducci et al.[62]), and possibly also the more spatially uniform flow field and cavitation activity spatial profiles attained at milliscales. These findings suggest that a larger number of crystal nuclei forms within the system at longer sonication times, for these give rise to longer transient cavitation activity (breakage, as discussed, does not take place).

Figure 13 shows the variation of yield versus the ultrasound duty cycle at the frequency of 42 kHz. The crystal yield is defined as

$$\text{yield}\ (\%) = \frac{\Delta m_{\text{filt}}}{\Delta m_{\text{eq}}} \times 100 \tag{19}$$

where Δm_{filt} is the mass of the collected crystals on the filter paper and Δm_{eq} is the maximum available mass in the supersaturated solution that potentially could crystallize (when equilibrium is reached at the given operating temperature). The graph shows an increase of yield with ultrasound duty cycle. This is attributed to the increase in the nucleation of the crystals under the action of ultrasound. During the period in which ultrasound is on, the instantaneous nucleation rate varies in time in the same way for any value of the duty cycle employed. This rate decreases drastically when ultrasound is off. Thus, crystals nucleate mainly when ultrasound is on. For larger values of the duty cycle, ultrasound is on for a longer fraction of the residence time, and so a larger number of nuclei generates. This results in a larger yield.

Ultrasound generates acoustic streaming, and this reduces the mass transfer resistance associated with the process of crystal growth. Nonetheless, the enhancement of the growth rate induced by ultrasound is not drastic. In particular, while ultrasound increases nucleation rates by several order of magnitudes, the order of magnitude of growth rates usually does not vary.[2] This is why we conclude that the duty cycle should have no bearing on crystal growth (the time that plays a role here is the residence time, which is the same for all experiments), and this is the reason we ascribe the increase in yield to the increase in the number of nuclei generated (over a time equal to the residence time of the crystallizer) as a

DOI: 10.1021/acs.cgd.6b00696
Cryst. Growth Des. XXXX, XXX, XXX−XXX

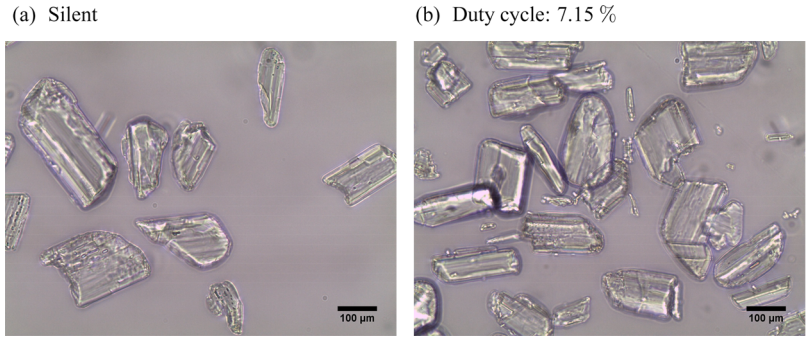

Figure 11. Adipic acid crystals collected after breakage experiments. (a) Silent and (b) duty cycle: 7.15% (6000 cycles).

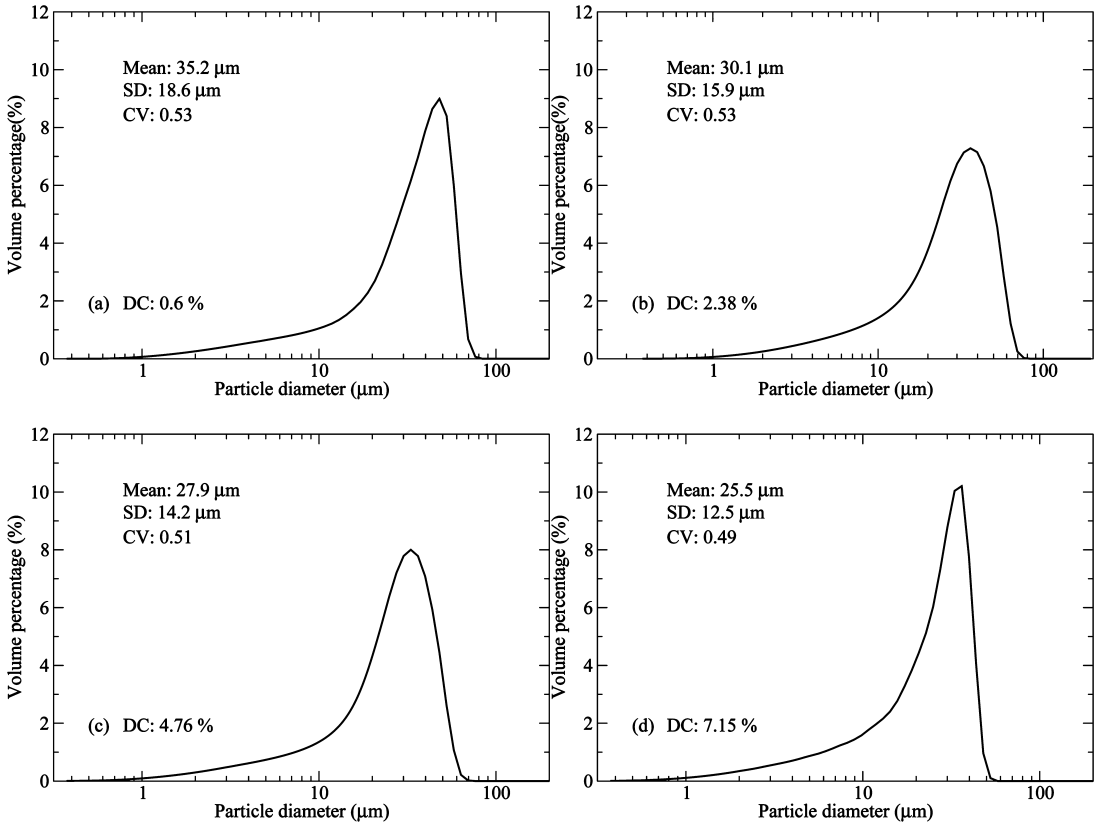

Figure 12. Crystal size distributions at different ultrasound duty cycle (a: 0.6%, b: 2.38%, c: 4.76% and d: 7.15%). S = 1.34. ν = 42 kHz. Amplitude = 400 mV_{PP}.

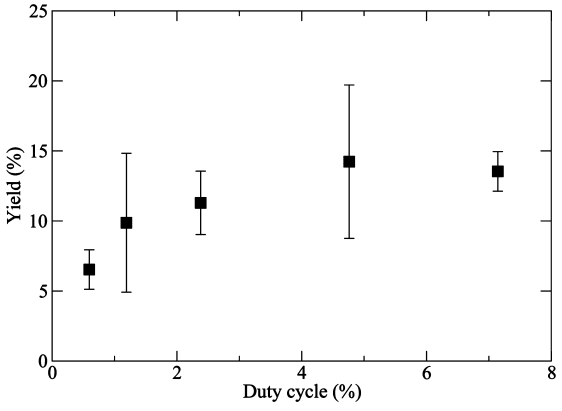

Figure 13. Crystal yield vs ultrasound duty cycle. S = 1.34. ν = 42 kHz. Amplitude = 400 mV_{PP}.

consequence of a longer use of ultrasound. It is worth mentioning that only a low percentage (maximum around 15% at the longest duty cycle) of all the available dissolved adipic acid was crystallized. The reason for low values of yield is probably due to the lack of a growth stage after the sonocrystallization unit. The residence time of the solution in our system is approximately 23 s, and hence the crystals may not have enough time for significant growth. Therefore, the magnitude of the yield is lower than that obtained in larger-scale sonocrystallization systems (such as the MSMPR used by Narducci et al.,[62] in which the residence time was 2 orders of magnitude longer). During the experiments, we observed that some of the crystals adhered to the walls of the channel. The mass of those crystals slightly decreased the value of the yield measured. However, the amount of crystals deposited at the wall was very small, and the increasing trend of the yield is not affected.

DOI: 10.1021/acs.cgd.6b00696
Cryst. Growth Des. XXXX, XXX, XXX−XXX

CONCLUSIONS

In this paper, a new continuous-flow, milliscale sonocrystallization device equipped with flat piezoelectric elements for production of adipic acid crystals is presented and studied. The device is able to produce crystals with a small mean size compared to other large-scale continuous sonocrystallization devices. The mean size of the crystals and the production rate (crystal yield) can be controlled by changing the duty cycle of ultrasound as well as its frequency. The mean size decreases by increasing the ultrasound duty cycle. This is because of longer periods of cavitation activity, which lead to more nucleation of crystals. To examine whether ultrasound affects crystal breakage, a set of experiments using seed crystals was conducted. The experiments reveal that in the presence of ultrasound the mean size and the morphology of crystals do not change. This indicates that the decrease in the mean size of crystals and the increase in the production rate under the action of ultrasound is due to more crystal nucleation. On the other hand, the mean crystal size increases by increasing the frequency of the wave, which is attributed to less transient cavitation activity at higher frequencies. To study the effect of frequency on transient cavitation activity, the probability of transient cavitation was investigated numerically by simulation of the wave propagation in the millichannel. By assuming a reasonable initial bubble nuclei size distribution and void fraction, the attenuating effect of cavitation bubbles was accounted for in the simulations. Furthermore, an acoustic Mach number above unity was set as the threshold for transient cavitation. The analysis shows that the expected zones for transient cavitation are predictable by numerical simulations. It is revealed that the transient cavitation activity is less likely at higher frequencies. Overall, it is concluded that transient cavitation of bubbles and its consequences are the most important mechanism for enhancing nucleation of crystals among the several proposed in the literature.

AUTHOR INFORMATION

Corresponding Author

*E-mail: l.mazzei@ucl.ac.uk.

Notes

The authors declare no competing financial interest.

ACKNOWLEDGMENTS

The authors thank The Engineering and Physical Sciences Research Council (EPSRC) of the UK for the financial support of this project under Grant Number EP/I031480/1. Fruitful discussions with the members of the R&D section of GlaxoSmithKline (GSK) is also acknowledged.

NOMENCLATURE

Latin letters

b damping factor [1/s]
c speed of sound [m/s]
C constant [$1/(\mu mm^3)$]
D gas thermal diffusivity [m^2/s]
f number density function [$1/(\mu m\ m^3)$]
h average element size [m]
H height [mm]
k wavenumber [1/m]
k_{em} electromechanical coupling factor [−]
k_m complex wavenumber [1/m]
L length [mm]
m mass [kg]
Ma Mach number [−]
n dimensionless number [−]
$\mathbf{n}$ surface normal unit vector [−]
N number of bubbles [−]
p acoustic pressure [Pa]
p_0 ambient pressure [Pa]
P acoustic pressure amplitude [Pa]
$\overline{P}$ complex conjugate of pressure amplitude [Pa]
Q_m mechanical damping factor [−]
$\mathbf{r}$ position vector in physical space [m]
R bubble radius [μm]
R_0 bubble radius at equilibrium [μm]
S supersaturation ratio [−]
SD standard deviation of distributions [μm]
t time [s]
$\mathbf{u}$ displacement vector [m]
V electrical potential [V]
W width [mm]

Greek letters

β volume fraction of bubbles [−]
γ specific heat ratio of gas [−]
δ dielectric loss or dissipation angle [deg]
η efficiency [−]
μ viscosity of liquid [Pa s]
ν frequency [Hz]
ρ density [kg/m^3]
σ surface tension [N/m]
$\boldsymbol{\tau}$ stress tensor [Pa]
Φ complex parameter [−]
χ dimensionless parameter [−]
ω wave frequency [rad/s]
ω_0 resonance frequency of bubbles [rad/s]

Subscripts

em electromechanical
eq equilibrium
filt filtered
g glass
G Gaussian
gas gaseous fluid
max maximum
mean mean value
min minimum
n normal
pp peak to peak
t time
w water
0 equilibrium, resonance

REFERENCES

(1) Shekunov, B.; York, P. *J. Cryst. Growth* **2000**, *211*, 122−136.
(2) Ruecroft, G.; Hipkiss, D.; Ly, T.; Maxted, N.; Cains, P. W. *Org. Process Res. Dev.* **2005**, *9*, 923−932.
(3) McCausland, L. J.; Cains, P. W.; Martin, P. D. *Chem. Eng. Prog.* **2011**97.
(4) Luque de Castro, M. D.; Priego-Capote, F. *Ultrason. Sonochem.* **2007**, *14*, 717−724.
(5) Wohlgemuth, K.; Ruether, F.; Schembecker, G. *Chem. Eng. Sci.* **2010**, *65*, 1016−1027.
(6) Guo, Z.; Jones, A. G.; Li, N. *Chem. Eng. Sci.* **2006**, *61*, 1617−1626.
(7) Lyczko, N.; Espitalier, F.; Louisnard, O.; Schwartzentruber, J. *Chem. Eng. J.* **2002**, *86*, 233−241.

DOI: 10.1021/acs.cgd.6b00696
Cryst. Growth Des. XXXX, XXX, XXX−XXX

(8) Miyasaka, E.; Kato, Y.; Hagisawa, M.; Hirasawa, I. *J. Cryst. Growth* **2006**, *289*, 324−330.
(9) Miyasaka, E.; Ebihara, E.; Hirasawa, I. *J. Cryst. Growth* **2006**, *295*, 97−101.
(10) Kordylla, A.; Koch, S.; Tumakaka, F.; Schembecker, G. *J. Cryst. Growth* **2008**, *310*, 4177−4184.
(11) Llinàs, A.; Goodman, J. M. *Drug Discovery Today* **2008**, *13*, 198−210.
(12) Narducci, O.; Jones, A. G.; Kougoulos, E. *Org. Process Res. Dev.* **2011**, *15*, 974−980.
(13) Narducci, O.; Jones, A. G. *Cryst. Growth Des.* **2012**, *12*, 1727−1735.
(14) Jiang, M.; Papageorgiou, C. D.; Waetzig, J.; Hardy, A.; Langston, M.; Braatz, R. *Cryst. Growth Des.* **2015**, *15*, 2486−2492.
(15) Flowers, B. S.; Hartman, R. L. *Challenges* **2012**, *3*, 194−211.
(16) Variankaval, N.; Cote, A. S.; Doherty, M. F. *AIChE J.* **2008**, *54*, 1682−1688.
(17) Chen, J.; Sarma, B.; Evans, J. M. B.; Myerson, A. S. *Cryst. Growth Des.* **2011**, *11*, 887−895.
(18) Jensen, K. F.; Reizman, B. J.; Newman, S. G. *Lab Chip* **2014**, *14*, 3206−3212.
(19) Teychené, S.; Biscans, B. *Chem. Eng. Sci.* **2012**, *77*, 242−248.
(20) Moschou, P.; de Croon, M. H.; van der Schaaf, J.; Schouten, J. C. *Rev. Chem. Eng.* **2014**, *30*, 127−138.
(21) Sultana, M.; Jensen, K. F. *Cryst. Growth Des.* **2012**, *12*, 6260−6.
(22) Gerdts, C. J.; Elliott, M.; Lovell, S.; Mixon, M. B.; Napuli, A. J.; Staker, B. L.; Nollert, P.; Stewart, L. *Acta Crystallogr., Sect. D: Biol. Crystallogr.* **2008**, *64*, 1116−22.
(23) Elvira, K. S.; Casadevall i Solvas, X.; Wootton, R. C. R.; de Mello, A. J. *Nat. Chem.* **2013**, *5*, 905−915.
(24) Marre, S.; Jensen, K. F. *Chem. Soc. Rev.* **2010**, *39*, 1183−1202.
(25) Nilsson, A.; Petersson, F.; Jönsson, H.; Laurell, T. *Lab Chip* **2004**, *4*, 131−135.
(26) Barnkob, R.; Augustsson, P.; Laurell, T.; Bruus, H. *Lab Chip* **2010**, *10*, 563−70.
(27) Neppiras, E. *Phys. Rep.* **1980**, *61*, 159−251.
(28) Fernandez Rivas, D.; Stricker, L.; Zijlstra, A. G.; Gardeniers, H. J. G. E.; Lohse, D.; Prosperetti, A. *Ultrason. Sonochem.* **2013**, *20*, 510−524.
(29) Jordens, J.; Gielen, B.; Braeken, L.; Van Gerven, T. *Chem. Eng. Process. Process Intensif.* **2014**, 1−7.
(30) Sander, J. R. G.; Zeiger, B. W.; Suslick, K. S. *Ultrason. Sonochem.* **2014**, *21*, 1908−15.
(31) Rossi, D.; Jamshidi, R.; Saffari, N.; Kuhn, S.; Gavriilidis, A.; Mazzei, L. *Cryst. Growth Des.* **2015**, *15*, 5519−5529.
(32) Mullin, J. *Crystallization*; Butterworth-Heinemann: Oxford, 2001.
(33) Louisnard, O. *Phys. Rev. E* **2008**, *78*, 036322.
(34) Saclier, M.; Peczalski, R.; Andrieu, J. *Ultrason. Sonochem.* **2010**, *17*, 98−105.
(35) Harzali, H.; Baillon, F.; Louisnard, O.; Espitalier, F.; Mgaidi, a. *Ultrason. Sonochem.* **2011**, *18*, 1097−106.
(36) Servant, G.; Laborde, J.; Hita, A.; Caltagirone, J. P.; Gerard, A. *Ultrason. Sonochem.* **2001**, *8*, 163−174.
(37) Neppiras, E. A. *Phys. Rep.* **1980**, *61*, 159−251.
(38) Neppiras, E. A. *Ultrasonics* **1980**, *18*, 201−209.
(39) Prosperetti, A. *Ultrasonics* **1984**, *22*, 69−77.
(40) Commander, K. W.; Prosperetti, A. *J. Acoust. Soc. Am.* **1989**, *85*, 732−746.
(41) Labouret, S.; Frohly, J. *Eur. Phys. J.: Appl. Phys.* **2002**, *19*, 39−54.
(42) Rozenberg, L. D. *High-Intensity Ultrasonic Fields*; Plenum Press: New York, 1971; Chapter: The Cavitation Zone.
(43) Dähnke, S.; Keil, F. J. *Ind. Eng. Chem. Res.* **1998**, *37*, 848−864.
(44) Mettin, R.; Akhatov, I.; Parlitz, U.; Ohl, C. D.; Lauterborn, W. *Phys. Rev. E: Stat. Phys., Plasmas, Fluids, Relat. Interdiscip. Top.* **1997**, *56*, 2924−2931.
(45) Ye, Z.; Ding, L. *J. Acoust. Soc. Am.* **1995**, *98*, 1629−1636.
(46) Nechibvute, A.; Chawanda, A.; Luhanga, P. *ISRN Mater. Sci.* **2012**, *2012*, 1−11.
(47) Piefort, V. Finite Element Modelling of Piezoelectric Active Structures. Ph.D. Thesis, Universite Libre de Bruxelles, 2001.
(48) Nygren, M. W. Finite Element Modeling of Piezoelectric Ultrasonic Transducers. Ph.D. Thesis, Norwegian University of Science and Technology, 2011.
(49) Popovici, D.; Constantinescu, F.; Maricaru, M.; Hantila, F.; Nitescu, M.; Gheorghe, A. *Recent Adv. Model. Simul.*; InTech: Rijeka, Croatia, 2008.
(50) Raman, V.; Abbas, A.; Joshi, S. *Proceedings of the COMSOL Users Conference*; Bangalore, India, 2006.
(51) Klima, J.; Ferrer, A. F.; Garcia, J. G.; Ludvik, J.; Saez, V.; I, J. *Ultrason. - Sonochem.* **2007**, *14*, 605−614.
(52) Babuska, I. M.; Sauter, S. A. *SIAM Rev.* **2000**, *42*, 451−484.
(53) Apfel, R. E. *J. Acoust. Soc. Am.* **1981**, *69*, 1624−1633.
(54) Keller, J. B.; Miksis, M. *J. Acoust. Soc. Am.* **1980**, *68*, 628−633.
(55) Wijngaarden, L. V. *Annu. Rev. Fluid Mech.* **1972**, *4*, 369−394.
(56) Ando, K.; Colonius, T.; Brennen, C. E. *J. Acoust. Soc. Am.* **2009**, *126*, EL69−EL74.
(57) Dähnke, S.; Keil, F. *Chem. Eng. Technol.* **1998**, *21*, 873−877.
(58) Jamshidi, R.; Pohl, B.; Peuker, U. A.; Brenner, G. *Chem. Eng. J.* **2012**, *189*−*190*, 364−375.
(59) Wu, J.; Zhu, Z.; Du, G. *Ultrasound Med. Biol.* **1995**, *21*, 545−552.
(60) Jordens, J.; De Coker, N.; Gielen, B.; Van Gerven, T.; Braeken, L. *Ultrason. Sonochem.* **2015**, *26*, 64−72.
(61) Clydesdale, G.; Thomson, G. B.; Walker, E. M.; Roberts, K. J.; Meenan, P.; Docherty, R. *Cryst. Growth Des.* **2005**, *5*, 2154−2163.
(62) Narducci, O.; Jones, A. G.; Kougoulos, E. *Chem. Eng. Sci.* **2011**, *66*, 1069−1076.

DOI: 10.1021/acs.cgd.6b00696
Cryst. Growth Des. XXXX, XXX, XXX−XXX